



Synthesis of Hierarchical Graphene-MnO₂ Nanowire Composites with Enhanced Specific Capacitance

T. VELDEVI¹, K. THILEEP KUMAR¹, R.A. KALAIVANI¹, S. RAGHU^{1,2} and A.M. SHANMUGHARAJ^{1,2,*}

¹Department of Chemistry, Vels Institute of Science Technology and Advanced Studies (VISTAS), Chennai-600117, India

²Centre for Energy and Alternative Fuels, Vels Institute of Science Technology and Advanced Studies (VISTAS), Chennai-600117, India

*Corresponding author: E-mail: shanmughar@gmail.com

Received: 8 January 2019;

Accepted: 15 March 2019;

Published online: 28 June 2019;

AJC-19440

Hierarchical nanostructured graphene–manganese dioxide nanowire (G-MnO₂-NW) composites have been prepared by hydrothermal synthesis route using water/1-decanol as the medium. Synthesized materials were analyzed using various characterization tools to corroborate their chemical compositions, structure/morphology and surface area. Electrochemical measurements of the synthesized G-MnO₂-NW electrode materials delivered the highest specific capacity (255 Fg⁻¹), high rate capability and improved cycling stability at 0.5 Ag⁻¹ in 1M sodium sulfate solution and this fact may be attributed to its high surface area and porosity. Moreover, synthesized G-MnO₂-NW electrodes displayed better energy and power density, when compared to the MnO₂-NW based electrodes.

Keywords: MnO₂ nanowire, Graphene, Supercapacitor electrode, Specific capacitance, Power density, Energy density.

INTRODUCTION

Lightweight, mechanically strong and highly efficient energy storage devices have attracted significant attention due to their potential applications in portable and wearable consumer electronics, including electronic paper, roll-up displays, flexible biosensors and implantable medical devices [1-6]. Among the many types of energy storage devices, supercapacitors, which also termed as ultracapacitors, having energy density greater than that of electrolytic capacitors (10 Wh Kg⁻¹) and can be safely charged or discharged in seconds with exceptionally long cycle life (> 100,000 cycles) [6-10]. However, the successful design of supercapacitors depends on the various parameters such as nature of electrode materials, electrolytes and the device architecture [9,10]. Owing to its excellent cycle life, carbon based nanomaterials are widely applied as the electrode materials in supercapacitors [1,11-14]. Till now, noteworthy progress has been made on the development of carbon nanostructured supercapacitor electrodes by understanding its charge storage mechanisms [13-17]. Among the various carbon nanostructures, two dimensional graphene nanosheets is claimed to be robust and captivating electrode material for supercapacitors due to its outstanding properties

such as high electrical conductivity, surface-to-volume ratio and extraordinary theoretical capacitance (550 Fg⁻¹) [18-21]. Since the first experimental report on the exceptional capacitance performance of graphene-based supercapacitors [22], its scientific and technological significance is now becoming more widely recognized [23]. However, despite of much effort, the performance of graphene-based supercapacitors, especially in terms of their power delivery, has not yet been remarkably improved.

In recent years, some energy storage materials that store and release energy through redox reactions have attracted increasing interest as flexible electrode materials, since they have higher specific capacitance than carbon materials [24,25]. Decoration onto graphene of pseudo capacitive materials such as manganese dioxide [26-30], ruthenium dioxide [31,32], titanium dioxide [33,34], cobalt oxide [35,36], nickel and zinc cobaltate (NiCo₂O₄/ZnCo₂O₄) [37,38], nickel hydroxide [Ni(OH)₂] [39] and cobalt nickel sulfide (CoNi₂S₄) [40] has led to significant improvements in electrode capacitance. Among the various reported pseudo capacitive materials, MnO₂ has attracted much attention due to its low cost, environmental friendliness and high theoretical specific capacitance [27]. By decorating the surfaces of graphene fibers with MnO₂, Zheng

et al. [41] and Chen *et al.* [42] have enhanced the electrochemical performance of graphene fiber-based electrodes. However, in the resulting materials, the capacitance of the hybrid fibers is mainly dominated by the pseudo capacitive behaviour induced by the MnO₂ coated on the graphene surface, while the double layer capacitance induced by graphene sheets is seldomly utilized due to the graphene agglomeration. Furthermore, owing to its low electronic conductivity, only thin surface layer of MnO₂ can participate in the redox reactions and additional rise of the mass loading of MnO₂ usually lead to increased electrode resistance, decreased specific capacitance and reduced MnO₂ utilization rate. Such unfavourable dependency on thickness is a critical issue for low-conductivity electrode materials resulting in poorer transport of electrons and/or ions [43]. Thus, increasing the loading content of MnO₂ without sacrificing its utilization rate is still challenging task. Thus, it is highly desirable to develop a scalable and low-cost approach to fabricate ideal MnO₂-graphene hybrid materials with outstanding flexibility, high conductivity, large specific surface area and excellent capacitance for supercapacitor applications.

Herein, hierarchically structured hybrid nanostructures of MnO₂ nanowires and graphene (G-MnO₂-NW) were fabricated by a simple hydrothermal synthesis route and were shown to yield excellent capacitive performance. The MnO₂ nanowires not only acted as effective spacers to inhibit the restacking of graphene nanosheets, thereby increasing the specific surface area (130.1 m² g⁻¹), but also provided pseudocapacitance that improved the overall performance. Meanwhile, the highly conductive graphene nanosheets wrapping the MnO₂ nanowires facilitated electron transport in the nanowires and thus ensured a high MnO₂ electrochemical utilization rate. The prepared G-MnO₂-NW based supercapacitor electrodes displayed better specific capacitance value (255 Fg⁻¹ @ 0.5 Ag⁻¹), cycling stability (90 % capacitance retention over 1000 cycles) and energy and power density (of up to 28.56 Wh Kg⁻¹ and 810 W kg⁻¹, respectively), when compared to MnO₂-NW electrodes.

EXPERIMENTAL

Preparation of graphene oxide: Graphene oxide (GO) was synthesized using natural graphite (Sigma-Aldrich) by means of an improved synthesis method suggested by Marcano *et al.* [44]. In this method, a 9:1 mixture of concentrated sulfuric acid/phosphoric acid (H₂SO₄/H₃PO₄, 540:60 mL) was added to the mixture of graphite flakes (5 g) and potassium permanganate (30 g). The reaction mixture exothermically heated itself from room temperature to 35–40 °C and was further heated to 50 °C under stirring condition for 12 h. The reaction mixture was then cooled to room temperature and poured onto a mixture of ice (~500 mL) and 30 % hydrogen peroxide (Alfa Aesar, 5 mL). The resulting product was washed sequentially with ethanol, water and acetone. The obtained product was dried at room temperature under a low vacuum of 40 mmHg, yielding a pale green powder [45].

Preparation of graphene-MnO₂ nanowire composites: All chemical reagents used are of analytical grade and were used without further purification. In a typical hydrothermal synthesis, the stoichiometric composition of graphene oxide

(0.25 g); manganese(II) acetate (Mn(CH₃COO)₂·4H₂O; 1.99 g), sodium sulfate (1.98 g) and ammonium persulfate ((NH₄)₂S₂O₈; 1.92 g) were added to the water/1-decanol mixture (110/70 mL) and subjected it to stirring for about 0.5 h. After stirring, the resulting solution was transferred into a Teflon-lined stainless steel autoclave, sealed and allowed to react by keeping it at 140 °C for 24 h in an oven. After the reaction, the autoclave was taken out and cooled to room temperature. The as-synthesized sample was washed with deionized water and dried at 60 °C to yield G-MnO₂-NW composites. For comparison purposes, pristine MnO₂ nanowires (MnO₂-NW) were synthesized by the similar procedure without the addition of graphene oxide.

Characterization and electrochemical measurements: X-ray diffraction studies of MnO₂-NW and G-MnO₂-NW nanowires were conducted using an X-ray diffractometer (M18XHF-SRA, Mac Science Co. Ltd., Japan) equipped with a CuKα radiation source operated at 40 kV and 40 mA. XRD patterns were obtained at room temperature while scanning at 1°/min in the 2θ range of 10–80°. Thermogravimetric analysis of MnO₂-NW and G-MnO₂-NW was conducted over the temperature range of 25–900 °C at the heating rate of 10 °C/min in air (TGA Q5000 IR/SDT Q600, TA Instruments). Surface analysis of MnO₂-NW and G-MnO₂-NW was conducted using a Perkin-Elmer 2000 FT-IR spectrophotometer (Perkin-Elmer Inc., USA). FT-IR characterization of nanowire samples pelletized in KBr was performed in transmission mode over the IR range of 4000–400 cm⁻¹. Surface compositions of and functional groups present in the nanowire samples were determined by means of X-ray photoelectron spectroscopy (K-Alpha, Thermo Electron). MnO₂-NW and G-MnO₂-NW were structurally characterized by means of Raman spectroscopy (RFS/100s, Bruker, Germany). Specific surface areas of the nanowire samples were determined by means of the BET method using a surface area analyzer (BEL Sorp-II mini, BEL Japan Co., Japan). Morphological characterization of nanowire samples was carried out by means of field emission scanning electron microscopy (FE-SEM, LEO SUPRA 55, Carl Zeiss, Germany) using the acceleration voltage of 15 kV and by means of TEM (Jeol JSM-2010, Japan) using the acceleration voltage of 200 kV. The nanowires were prepared for TEM measurements by dispersing them in ethanol, depositing them onto a carbon-coated copper grid and drying them under vacuum.

The electrochemical performance of MnO₂-NW and G-MnO₂-NW was evaluated in three electrode systems. Working electrodes for three electrode measurements were prepared by casting a slurry composed of 80 wt. % active material (MnO₂-NW & G-MnO₂-NW), 10 wt. % of conductive carbon black (Super P, TIMCAL) as an additional conductive agent and 10 wt. % of poly(vinylidene difluoride) (Kureha KF100) as a binder onto stainless steel grid acting as the current collector. Slurry was prepared by grinding the mixture in the presence of N-methyl pyrrolidone solvent for 15 min using a mortar. The stainless steel grid coated with the viscous slurry was dried at 70 °C for 10 h in an oven. The active material mass loading in the prepared working electrodes was ~1.0 mg cm⁻². The electrochemical performances of the prepared materials were evaluated in three electrode assembly using platinum and Ag/AgCl electrode as counter electrode and reference electrode

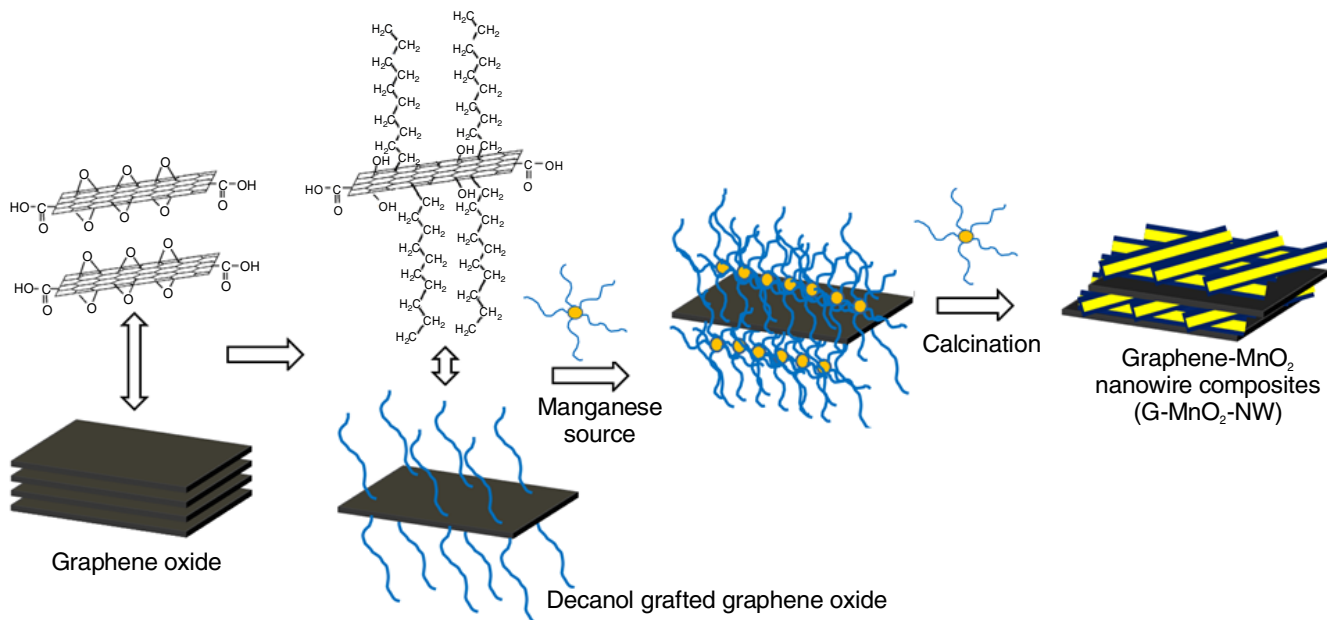


Fig. 1. Schematic representation of proposed synthesis steps of G-MnO₂-NW composites

in 1.0 M Na₂SO₄ aqueous solution. The working electrode with active mass loading of $\sim 1.0 \text{ mg cm}^{-1}$ for two electrode measurements was prepared by casting the slurry mixture onto nickel foam and subsequent drying at 70 °C for 10 h in an oven. Dried coated electrodes were pressed under a 7T load and then punched out into a desired size. Electrochemical properties of two and three electrode configurations were studied using galvanostatic charge–discharge measurements conducted in the voltage range of 0.01–1.0 V using a battery analyzer (WonA tech). Cyclic voltammetry measurements were carried out at 5–100 mV s⁻¹ in the voltage range of 0.01 to 1.0 V using an electrochemical workstation (VersaSTAT 3 Electrochemical System). EIS studies of the fabricated supercapacitors were also performed using the electrochemical workstation, by applying sine waves of amplitude 5.0 mV over the frequency range of 100 kHz to 0.01 Hz.

RESULTS AND DISCUSSION

Fig. 1 is the schematic representation of hydrothermally synthesized G-MnO₂-NW composites using water/1-decanol as the medium. The graphene oxide synthesized from natural graphite by means of the synthesis method used herein is a nonstoichiometric material consisting of many oxygen functionalities such as phenolic –OH, epoxy, carbonyl and carboxylic acid groups present both on the basal planes and along the edges [45–48]. In contrast to earlier reports on graphene-MnO₂ composites, we observed planar orientations of MnO₂ nanowires on the graphene surface. Though the exact reason is unknown, it is expected that epoxy groups present in the basal plane of the prepared graphene oxide undergo ring opening reactions with the 1-decanol solvent during the hydrothermal synthesis as depicted in Fig. 1. Simultaneously, the manganese salt reacts with the 1-decanol solvent leading to the formation of MnO₂ nuclei as proposed in Fig. 1. Hydrophobic interactions between the 1-decanol grafted onto both the MnO₂ nuclei and the graphene oxide are thought to act as a structure-directing

group that leads to the formation of MnO₂ nanowires with preferential planar orientation on the graphene surface, as proposed in Fig. 1.

To gain more insight into the crystalline nature of the MnO₂ nanowires formed on the graphene surface, XRD characterization was carried out over the 2θ range of 10°–70° (Fig. 2). Pristine graphene oxide showed a strong XRD peak at 2θ of 9.7° [45]. Contrastingly, several peaks appearing at the 2θ values of 12.5°, 17.7°, 28.6°, 37.5°, 41.7°, 49.6°, 55.6°, 59.8°, 65.2° and 68.8° were attributed to the (110), (200), (310), (211), (301), (411), (600), (521), (002) and (541) planes of α-MnO₂ (JCPDS card number 44-0141), indicating the formation of α-MnO₂ crystals in the nanowires. Also, the appearance of a new peak at $\sim 25^\circ$ corresponding to (002) diffraction of graphite, along with peaks of α-MnO₂ crystals, clearly indicates the presence of graphene in the G-MnO₂-NW system. The appearance of the graphite (002) peak in the G-MnO₂-NW samples revealed the presence of few layered graphene sheets in this system.

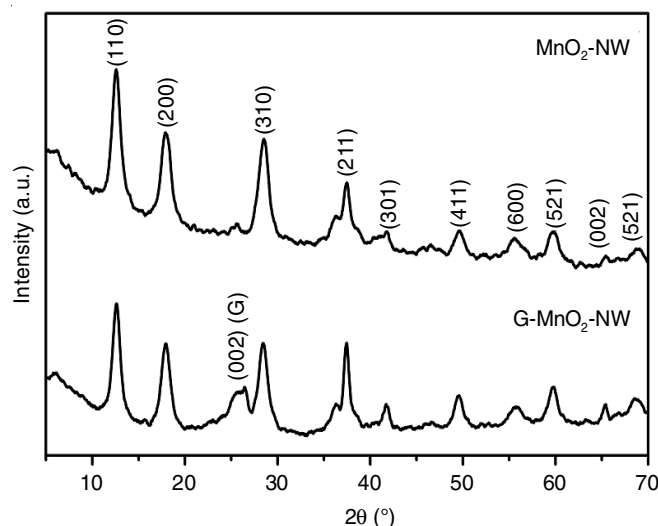


Fig. 2. X-ray diffraction results of MnO₂-NW and G-MnO₂-NW

The surface chemical composition of the G-MnO₂-NW material was determined using Fourier transform infrared spectroscopy (FT-IR). Pristine graphene oxide showed major IR stretching vibrations at 1710, 1630, 1217 and 1050 cm⁻¹, which respectively correspond to the C=O stretching (–COOH group), C–C stretching (aromatic group), C–O stretching (C–OH group) and C–O–C stretching (epoxy group) vibrations [45]. The MnO₂-NW samples showed peaks at 3700 cm⁻¹ (–OH stretching of MnO₂ nanowires), 730 cm⁻¹ (Mn–O–Mn stretching mode of MnO₆ core) and 520 cm⁻¹ (Mn–O stretching vibration of MnO₆ core). Alternatively, G-MnO₂-NW samples showed peaks at 3710 cm⁻¹ (–OH stretching of MnO₂ nanowires), 3540 cm⁻¹ (O–H stretching of phenolic groups in graphene), 2980 cm⁻¹ (C–H asymmetric stretching), 2875 cm⁻¹ (C–H symmetric stretching), 1590 cm⁻¹ (C=C stretching in graphene) along with peaks attributed to the MnO₂ nanowires.

To gain more insight into the surface chemical composition of the G-MnO₂ nanowires, they were subjected to XPS characterization and the results are given in Fig. 3. XPS survey scan results of the pristine graphene oxide showed two strong peaks at 285 and 530 eV, respectively corresponding to the C1s and O1s transitions (Fig. 3a). Alternatively, MnO₂-NW showed Mn2p (642 eV) and O1s (530 eV) peaks, along with a small C1s peak (285 eV). Formation of hierarchical G-MnO₂-NW composites was indicated by the significant rise observed in the C1s peak relative to that of MnO₂-NW, along with the appearance of Mn2p (642 eV) and O1s (530 eV) peaks. This conclusion is further supported by the relative increase in C/O peak intensity from 0.39 for MnO₂-NW to 0.73 for G-MnO₂-NW. High-resolution Mn2p spectra of both MnO₂-NW and G-MnO₂-NW materials showed two symmetrical peaks at ~641.8 and ~653.3 eV, attributed to Mn 2p_{1/2} and Mn 2p_{3/2} spin-orbit coupling of MnO₂ nanostructures. The resulting

high-resolution scans of Mn 2p_{1/2} and Mn 2p_{3/2} in both MnO₂-NW and G-MnO₂-NW samples were fitted with twelve Gaussian–Lorentz peaks, P1–P12 (Fig. 3a,b). The fitted peaks P1–P6 correspond to 2p_{1/2} spin-orbit coupling of Mn⁴⁺ (P1, P2), Mn³⁺ (P3, P4) and Mn²⁺ (P5, P6), whereas the fitted peaks P7–P12 correspond to 2p_{3/2} spin-orbit coupling of Mn⁴⁺ (P7, P8), Mn³⁺ (P9, P10) and Mn²⁺ (P11, P12). High-resolution C1s spectra of graphene oxide showed five components at around 284.5, 285.3, 286.9, 287.7 and 288.4 eV, which can be generally assigned to C–C/C–H, C–OH, C–O, C=O and O–C=O respectively (Fig. 3b); MnO₂-NW showed four major peaks at around 284.5, 286, 287.3 and 288.2 eV, respectively attributed to C–C/C–H, C–O, C=O and O–C=O (Fig. 3c). Interestingly, no additional peaks were observed for the G-MnO₂-NW composites compared to those observed for the MnO₂-NW samples, though the peak intensities did differ (Fig. 3d). Dramatic decreases were observed in the intensities of the C1s components associated with carbon–oxygen bonds (C–O groups) of graphene oxide in G-MnO₂-NW samples, attributed to the reduction of graphene oxide by manganese (Mn²⁺) ions generated during the hydrothermal reaction. The successful formation of MnO₂-NW and G-MnO₂-NW was further evidenced by deconvolutions of the O1s peaks of graphene oxide, MnO₂-NW and G-MnO₂-NW (Fig. 3e, 3f and 3g, respectively). In contrast to pristine graphene oxide, which showed two peaks corresponding to the C=O (532.0 eV) and C–O (533.0 eV) groups (Fig. 3e), peaks observed at ~529 eV (Mn–O–Mn) and 531 eV (Mn–O–C), along with a peak due to C–O–C groups (at 533.0 eV) evidenced the successful formation of MnO₂, in the cases both of MnO₂-NW and G-MnO₂-NW (Fig. 3e, f).

Raman spectrum of pure graphene oxide included a D-band peak (K-point phonons of A_{1g} symmetry) at 1354 cm⁻¹, typically assigned to defects and disordered structures of the

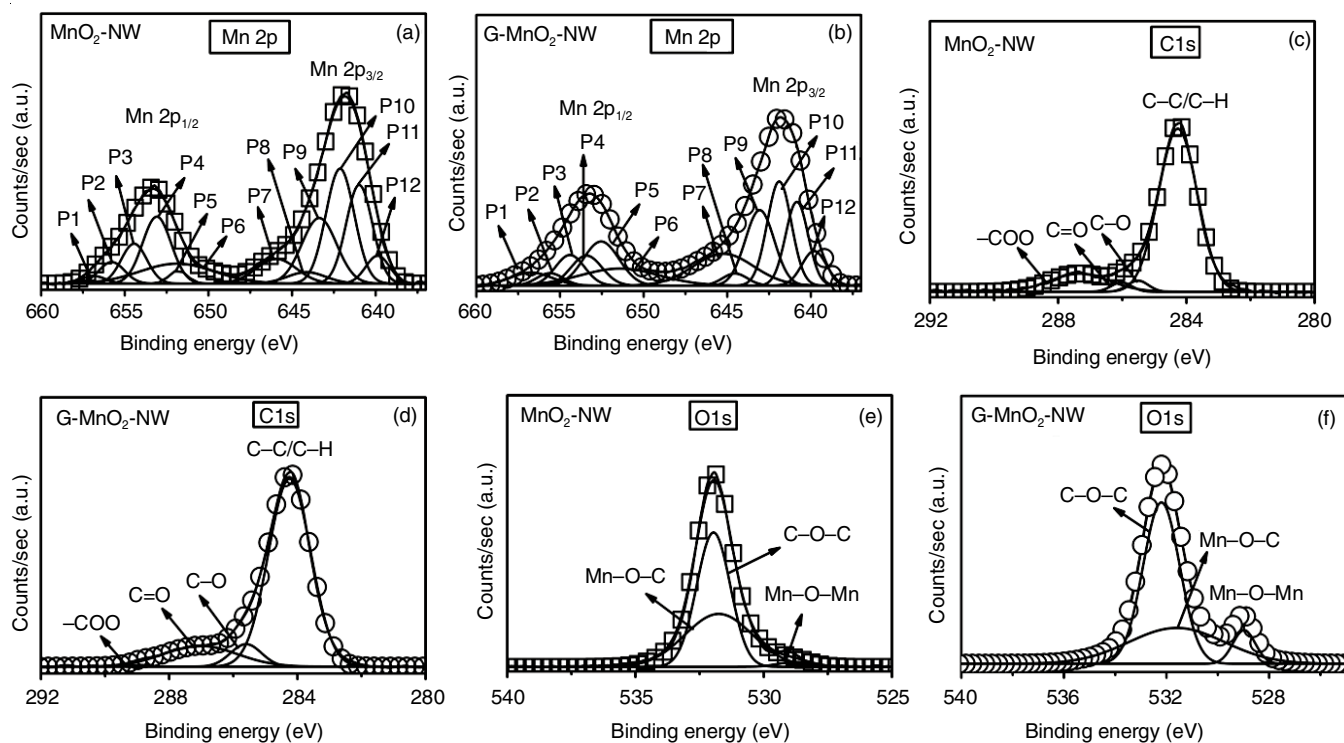


Fig. 3. XPS spectra of MnO₂-NW and G-MnO₂-NW

graphene oxide lattice. Another peak observed at 1586 cm⁻¹ was assigned to the G band (E_{2g} phonon of carbon), arising from the vibration of sp²-bonded carbon atoms in the hexagonal lattice of graphene oxide. In comparison, the D and G Raman bands of the G-MnO₂-NW material were located at different positions, 1350 and 1590 cm⁻¹ respectively. A systematic literature search revealed that metal oxide nanoparticles deposited on a graphene oxide surface usually increase the ratio of D and G band intensities (I_D/I_G), supporting the assumption that there is an electronic interaction between the nanowires and graphene. In the present investigation, the intensity ratio of G-MnO₂-NW (I_D/I_G = 1.10) was larger than that of the pure graphene oxide (I_D/I_G = 0.92), indicating a decrease of sp² domains in the former due to the presence of planar MnO₂ nanowires on the graphene layers [49]. Additionally, the G-band peak position was hypsochromically shifted from 1584 cm⁻¹ for graphene oxide to 1590 cm⁻¹ for G-MnO₂-NW, corroborating the p-type doping effect (*i.e.*, electron withdrawal) of MnO₂ nanowires on graphene [50]. In addition, the appearance of two sharp Raman bands at 574 cm⁻¹ and at 640 cm⁻¹ in the G-MnO₂-NW samples indicated the formation of a well-developed tetragonal structure with a (2 × 2) tunnel [51,52]. The size of the (2 × 2) tunnel is about 0.46 nm, which is suitable for intercalation–deintercalation of electrolyte cations; this may be the reason for the high pseudo capacitive behaviour of the synthesized material [53].

FE-SEM micrographs were acquired of MnO₂-NW and of G-MnO₂-NW prepared using graphene oxide and the results are included in Fig. 4. A low-magnification SEM image of MnO₂-NWs showed that these nanowires had interconnected porous network morphology, as revealed in the high-magnification SEM image (Fig. 4). Similarly, G-MnO₂-NW consisted of randomly oriented MnO₂ nanowires of porous network morphology impregnated on the graphene surface (Fig. 4). The observed SEM results agreed well with the results reported by various research groups on MnO₂ nanowires and their composites with graphene [54–57]. In contrast to the pristine graphene oxide [45], which had a wrinkled morphology (micrograph not shown), a plate-like morphology with several impregnated nanowire structures was observed on G-MnO₂-NW samples, confirming the successful formation of hierarchical MnO₂ nanowires on the graphene oxide surface (Fig. 4).

To gain more insight into the morphological features of MnO₂-NW and G-MnO₂-NW, they were characterized by field emission transmission electron microscopy (Fig. 5). Low and high-magnification TEM images of a MnO₂-NW sample revealed that the synthesized nanowires were tens of micrometers long and 20 nm in diameter on average. G-MnO₂-NW was found to consist of a hierarchical structure of MnO₂ nanowires impregnated between the graphene nanosheets (Fig. 5).

Table-1 includes the surface areas calculated by means of the BET method from nitrogen adsorption–desorption curves.

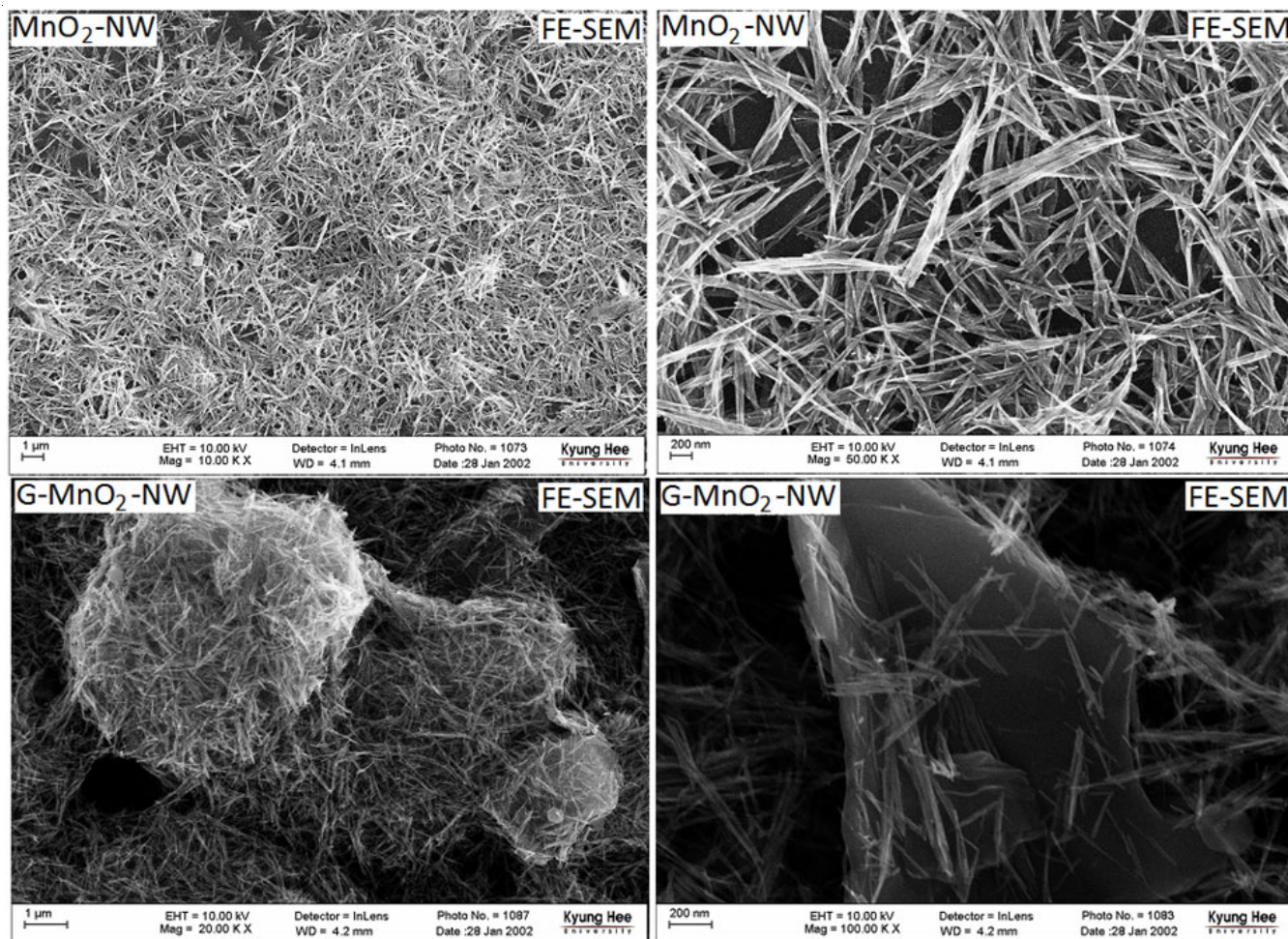


Fig. 4. FE-SEM micrographs of MnO₂-NW and G-MnO₂-NW

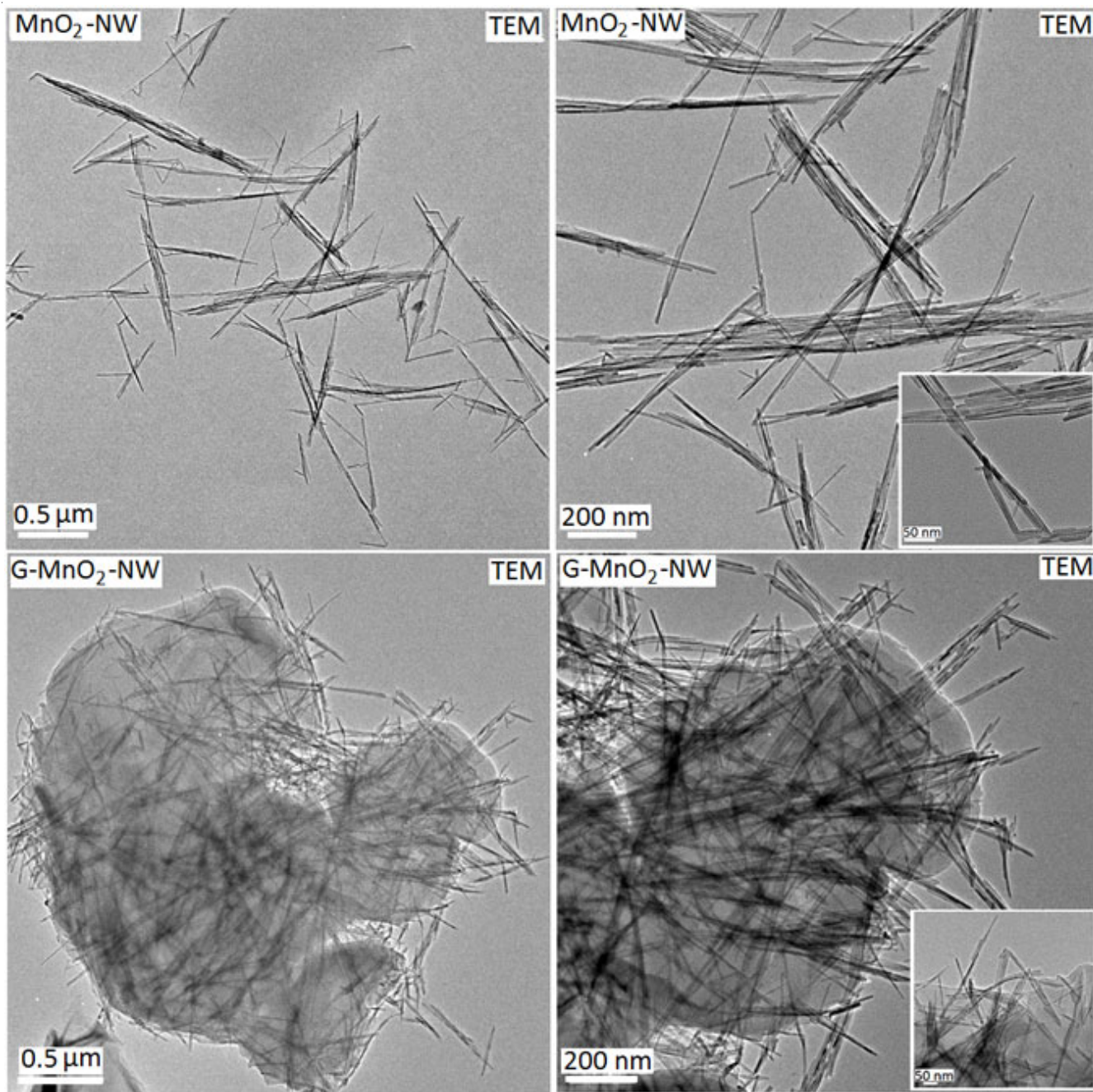


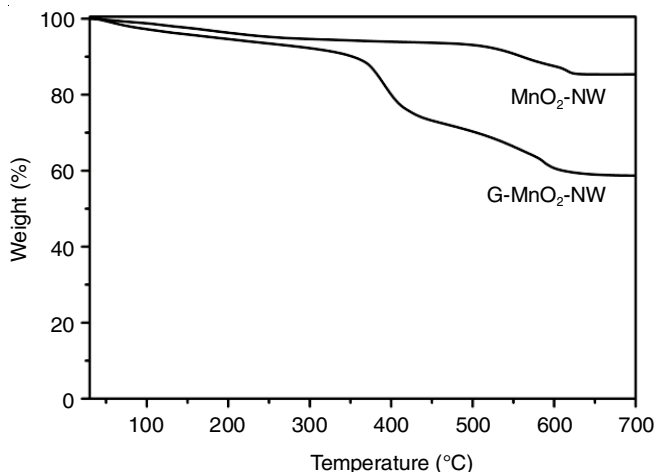
Fig. 5. Transmission electron micrographs of MnO₂-NW and G-MnO₂-NW

The surface areas of graphene oxide and MnO₂-NW were thus calculated to be 48.5 and 62 m² g⁻¹, respectively. Significant improvement in surface area (130.1 m² g⁻¹, 110 % increment) was noted for the G-MnO₂-NW composites, relative to the MnO₂-NW. Pore size distributions and average pore sizes were estimated based on the Barrett–Joyner–Halenda (BJH) method. The broad pore size distribution and average pore sizes of MnO₂-NW (distribution, 3–75 nm; average, 5 nm) and G-MnO₂-NW (distribution, 3–88 nm; average, 8 nm) were slightly lower than those of graphene oxide (distribution, 3–90.2 nm; average, 17.3 nm) corroborating their mesoporous nature. It can be interpreted from these results that the high BET surface area and low porosity of the long MnO₂ nanowire architecture can provide shortened diffusion paths for electrons and ions, which can enhance supercapacitor performance [56].

TABLE-1
PREPARED ACTIVE SAMPLES BET RESULTS

Samples	BET N ₂ surface area (m ² g ⁻¹)	Average pore size (nm)	Pore size distribution (nm)
Graphene oxide	48.5	17.3	3~90.2
MnO ₂ -NW	62.0	5.0	3~75.0
G-MnO ₂ -NW	130.1	8.0	3~88.0

Thermogravimetric analysis was employed to determine the weight composition of the MnO₂ nanowires in the G-MnO₂-NW composites (Fig. 6). In the present work, weight loss of ~15 wt. % was observed in the temperature range of 30–700 °C for MnO₂-NW samples. These observed weight losses can be divided into three steps [58]: (i) ~5 % weight loss occurred in the temperature range of 30–300 °C owing to the loss of physisorbed water,

Fig. 6. TGA traces of MnO₂-NW and G-MnO₂-NW

(ii) ~2 % weight loss occurred in the temperature range of 300–500 °C owing to the loss of chemisorbed oxygen and water, (iii) ~8 % weight loss occurred in the temperature range of 500–700 °C owing to the reduction of manganese oxide as well as the loss of carbon coated on the MnO₂-NW samples. In contrast, the relatively greater weight loss observed over the entire temperature range for G-MnO₂-NW was attributed to the degradation of graphene sheets upon their exposure to air. The residual weight

of MnO₂-NW was 85 % and that of G-MnO₂-NW was 42 %; the difference was attributed to the difference in MnO₂ concentration between these two samples (Fig. 6).

To further explore the potential applications of MnO₂-NW and G-MnO₂-NW in energy storage applications, these materials were used to fabricate supercapacitor electrodes and its electrochemical performance were evaluated in three electrode configuration using cyclic voltammogram and galvanostatic charge–discharge measurements (Fig. 7). Fig. 7a shows the cyclic voltammograms acquired for G-MnO₂-NW samples within the electrochemical window from 0.01 to 1.0 V at different scan rates (5, 10, 20, 50 and 100 mV s⁻¹). For comparison purpose, cyclic voltammogram of MnO₂-NW was carried out at a selective scan rate (20 mV s⁻¹). The ideal pseudo capacitive behaviour of the MnO₂-NW electrode is well corroborated by the appearance of quasi rectangular CV curve. Owing to its high surface area and nanowire structure, MnO₂-NW provides well-ordered tunnels for the convenient insertion/extraction of ions during electrochemical cycling. The electrochemical reaction between the electrode and Na⁺ ions of the electrolyte [26] can be expressed as follows [59]:



In contrast to MnO₂-NW, appearance of quasi-symmetric curves with relatively higher loop area for G-MnO₂-NW

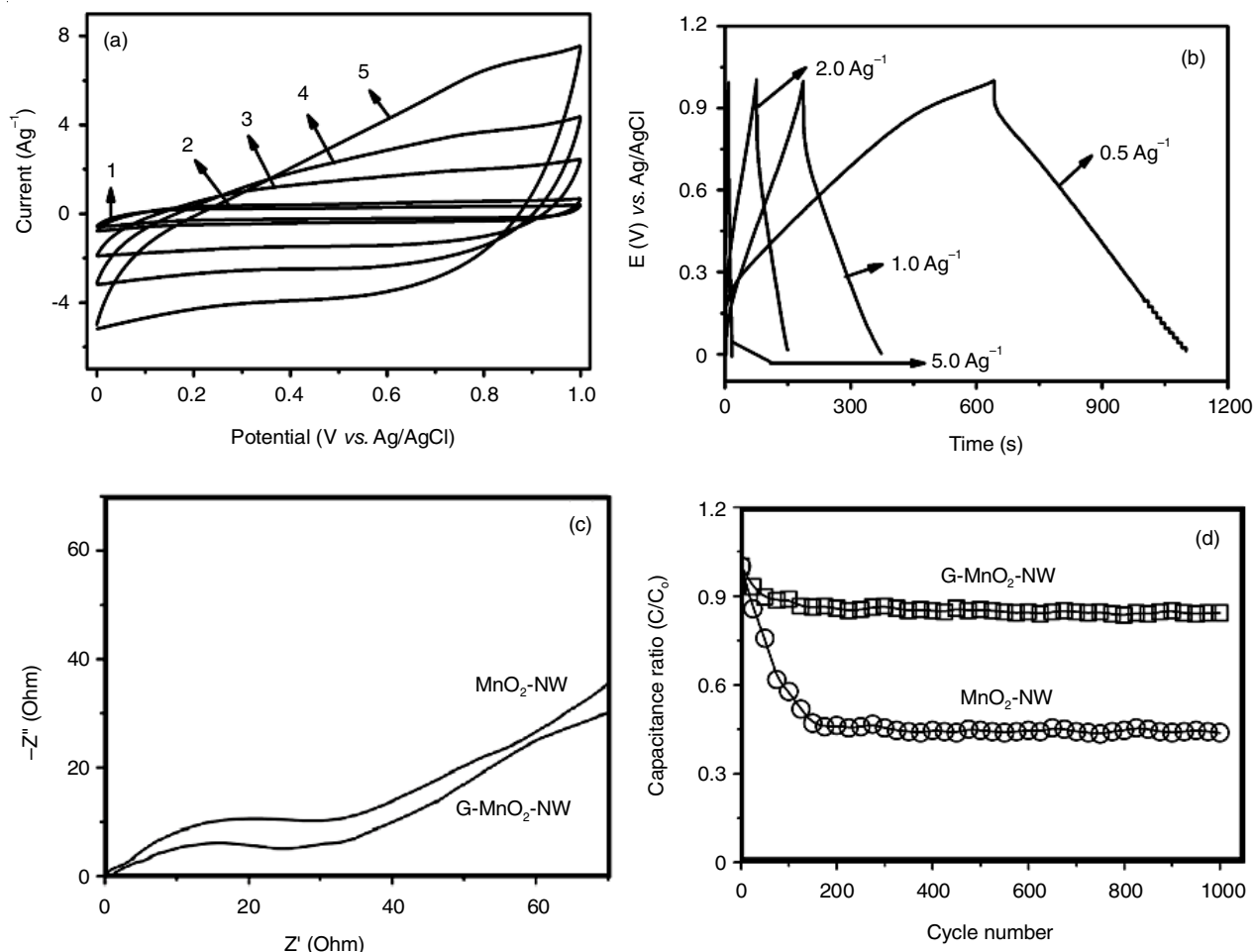


Fig. 7. Electrochemical characterization results of MnO₂-NW and G-MnO₂-NW based supercapacitor electrodes: (a) cyclic voltammograms of G-MnO₂-NW-based supercapacitors; (b) first charge–discharge profiles; (c) electrochemical impedance plots; (d) 1000-cycle capacity retention profiles

electrodes revealed the combined effect of double-layer and pseudo capacitive contribution to the total capacitance value corroborating the synergistic contribution of both graphene and MnO₂ nanowires. The unique microstructure as depicted in Fig. 1 provides (a) efficient pathway with improved diffusion rate of Na⁺ in its bulk state (b) nanowire structure of MnO₂ drastically reduce the diffusion length during charge/discharge process and thereby improves the MnO₂ utilization rate (c) presence of graphene nanosheets enhances the fast electron transfer throughout the electrode due to its excellent interfacial contact. As expected, loop area increased with increasing scan rate for G-MnO₂-NW electrodes (Fig. 7a) corroborating the enhanced charge transfer process.

Since, the discharge current in cyclic voltammetry is not always constant over the entire potential window, galvanostatic charge–discharge measurements are often used for calculating the specific capacitance of an electrode. The charge storage behaviour of the G-MnO₂-NW electrodes was thus measured under the various current densities (0.5–5 Ag⁻¹) using 1 M Na₂SO₄ as the electrolyte (Fig. 7b); the resulting curves were highly linear and symmetrical at all current densities, demonstrating stable electrochemical reversibility. For comparison purpose, galvanostatic charge–discharge measurements of MnO₂-NW electrodes was carried out at a selective current density (0.5 Ag⁻¹). The hierarchical G-MnO₂-NW composite electrodes displayed excellent charge–discharge characteristics and good current–voltage response, revealing their excellent capacitive characteristics, when compared to the MnO₂-NW electrodes. Based on galvanostatic charge–discharge curves, the specific capacitance (C, Fg⁻¹) at different current densities can be calculated by using the following equation:

$$C = \left(\frac{I \times \Delta t}{\Delta V \times m} \right) \quad (2)$$

where I, ΔV, Δt and m respectively represent the discharge current (A), the voltage change ignoring the small potential drop (V), the discharge time (s) and the mass of the active electrode material (*i.e.*, MnO₂-NW or G-MnO₂-NW) in one electrode (g), respectively [60,61]. The specific capacitance values of the G-MnO₂-NW supercapacitor electrodes are observed to be 255, 210, 160, 56 Fg⁻¹ on increasing current rates from 0.5–5 Ag⁻¹. The synergistic contribution of graphene and MnO₂ nanowires on the electrochemical performances is well corroborated by the significant rise in specific capacitance for G-MnO₂-NW (255 Fg⁻¹ at 0.5 Ag⁻¹), when compared to the MnO₂ nanowire electrode (150 Fg⁻¹ at 0.5 Ag⁻¹). This result is quite consistent with previous reports published by various research groups on graphene/MnO₂ composites [62–65]. The fabricated supercapacitor electrodes using the G-MnO₂-NW composites yielded greater gravimetric energy (28.56 Wh kg⁻¹) and power density (812 W kg⁻¹) compared to the MnO₂-NW based electrodes (energy density, 18.8 Wh kg⁻¹; power density, 251 W kg⁻¹).

EIS measurements were carried out over the frequency range from 100 kHz to 0.1 Hz to understand its electrochemical performances. The resulting impedance plots of the supercapacitor electrodes fabricated using MnO₂-NW and G-MnO₂-NW electrodes each consisted of a semicircle in the high-frequency region and nearly vertical line in the low-frequency

region (Fig. 7c). The equivalent series resistance (R_s) of the electrode and the charge-transfer resistance (R_{ct}) of the electrode–electrolyte interface are represented by the intersection on the real axis and the diameter of the semicircle, respectively [66,67]. G-MnO₂-NW had a considerably smaller R_{ct} than MnO₂-NW (~57 % decrement), indicating the formation of a hierarchical G-MnO₂-NW composite structure that increased the distance between the graphene sheets. This promoted ion diffusion within the electrode materials, thereby facilitating efficient utilization of the active materials.

To confirm the electrochemical stability of the MnO₂-NW and G-MnO₂-NW electrodes, the supercapacitor electrodes were subjected to 1000 charge–discharge cycles performed between 0.01 and 1.0 V under the current density of 0.5 Ag⁻¹ (Fig. 7d). After 1000 cycles, the supercapacitor electrodes fabricated using G-MnO₂-NW electrodes displayed ~90 % capacity retention, greater than the ~70 % retention observed for those based on MnO₂-NW. The unique nanosheet–nanowire structure of the G-MnO₂-NW composite effectively prevented the aggregation of graphene and MnO₂ nanowires during cycling and consequently provided high specific surface area, which is favourable for fast transport of hydrated ions in the electrolyte to the surfaces of both the graphene and the MnO₂ nanowires. Furthermore, the superior electrical conductivity of graphene can significantly decrease the internal resistance of the electrode by means of the construction of a conductive network. MnO₂ nanowires with small diameters also facilitate short ion diffusion paths, which can greatly reduce charge-transfer resistance and ionic diffusion resistance [55,62].

Conclusion

Novel hierarchical graphene–MnO₂ nanowire (G-MnO₂-NW) composites were synthesized *via* hydrothermal synthesis using a water/1-decanol mixture as the medium. The formation of high-surface-area graphene–MnO₂ nanowire composites was confirmed by means of FT-IR, XPS, FE-SEM, TEM and BET analyses. Supercapacitor electrodes fabricated using the G-MnO₂-NW composites as the electrode materials demonstrated high capacitance (255 Fg⁻¹ at 0.5 Ag⁻¹) and good stability during charge–discharge cycling (10 % decay after 1000 cycles), performance superior to supercapacitors fabricated using the MnO₂ nanowire (MnO₂-NW) system. Moreover, G-MnO₂-NW-based supercapacitors possessed higher energy density (28.56 Wh kg⁻¹) and better power density (812 W kg⁻¹) than the MnO₂-NW-based supercapacitor electrodes. We believe that graphene and graphene-based composites have great potential application for hybrid electric vehicles and electric vehicles, which strongly require high-power and high-energy storage systems.

ACKNOWLEDGEMENTS

The authors express their gratitude to DST/SERB-Project (Ref. no: DST/ECR/SERB/000815-2017) & DST/MES- project (Ref. no: DST/TMD/MES/2k17/039-2017).

CONFLICT OF INTEREST

The authors declare that there is no conflict of interests regarding the publication of this article.

REFERENCES

- S.R. Srither, A. Karthik, S. Arunmetha, D. Murugesan and V. Rajendran, *Mater. Chem. Phys.*, **183**, 375 (2016); <https://doi.org/10.1016/j.matchemphys.2016.08.041>.
- K. Jost, D. Stenger, C.R. Perez, J.K. McDonough, K. Lian, Y. Gogotsi and G. Dion, *Energy Environ. Sci.*, **6**, 2698 (2013); <https://doi.org/10.1039/c3ee40515j>.
- Z. Weng, Y. Su, D.W. Wang, F. Li, J. Du and H.M. Cheng, *Adv. Energy Mater.*, **1**, 917 (2011); <https://doi.org/10.1002/aenm.201100312>.
- D.S. Su and R. Schlögl, *ChemSusChem*, **3**, 136 (2010); <https://doi.org/10.1039/c9cc30090182>.
- J. Bae, J.Y. Park, O.S. Kwon and C.-S. Lee, *J. Ind. Eng. Chem.*, **51**, 1 (2017); <https://doi.org/10.1016/j.jiec.2017.02.023>.
- L.L. Zhang and X.S. Zhao, *Chem. Soc. Rev.*, **38**, 2520 (2009); <https://doi.org/10.1039/b813846j>.
- R. Rajagopal and K.-S. Ryu, *J. Ind. Eng. Chem.*, **60**, 441 (2018); <https://doi.org/10.1016/j.jiec.2017.11.031>.
- J.R. Miller and P. Simon, *Science*, **321**, 651 (2008); <https://doi.org/10.1126/science.1158736>.
- X. Xiao, T. Li, P. Yang, Y. Gao, H. Jin, W. Ni, W. Zhan, X. Zhang, Y. Cao, J. Zhong, L. Gong, W.C. Yen, W. Mai, J. Chen, K. Huo, Y.L. Chueh, Z.L. Wang and J. Zhou, *ACS Nano*, **6**, 9200 (2012); <https://doi.org/10.1021/nn303530k>.
- X. Zhang, X. Sun, H. Zhang, D. Zhang and Y. Ma, *Mater. Chem. Phys.*, **137**, 290 (2012); <https://doi.org/10.1016/j.matchemphys.2012.09.023>.
- C. Liu, F. Li, L.P. Ma and H.M. Cheng, *Adv. Mater.*, **22**, E28 (2010); <https://doi.org/10.1002/adma.200903328>.
- Y. Zhai, Y. Dou, D. Zhao, P.F. Fulvio, R.T. Mayes and S. Dai, *Adv. Mater.*, **23**, 4828 (2011); <https://doi.org/10.1002/adma.201100984>.
- Y. Liu, D. He, J. Duan, Y. Wang and S. Li, *Mater. Chem. Phys.*, **147**, 141 (2014); <https://doi.org/10.1016/j.matchemphys.2014.04.020>.
- I.I. Gurten Inal, S.M. Holmes, E. Yagmur, N. Ermumcu, A. Banford and Z. Aktas, *J. Ind. Eng. Chem.*, **61**, 124 (2018); <https://doi.org/10.1016/j.jiec.2017.12.009>.
- Z.S. Wu, K. Parvez, X. Feng and K. Müllen, *Nat. Commun.*, **4**, 2487 (2013); <https://doi.org/10.1038/ncomms3487>.
- A.S. Arico, P. Bruce, B. Scrosati, J.M. Tarascon and W. Van Schalkwijk, *Nat. Mater.*, **4**, 366 (2005); <https://doi.org/10.1038/nmat1368>.
- X.Y. Lang, A. Hirata, T. Fujita and M.W. Chen, *Nat. Nanotechnol.*, **6**, 232 (2011); <https://doi.org/10.1038/nnano.2011.13>.
- J.R. Miller, R.A. Outlaw and B.C. Holloway, *Science*, **329**, 1637 (2010); <https://doi.org/10.1126/science.1194372>.
- J.L. Xia, F. Chen, J.H. Li and N.J. Tao, *Nat. Nanotechnol.*, **4**, 505 (2009); <https://doi.org/10.1038/nnano.2009.177>.
- M.F. El-Kady, V. Strong, S. Dubin and R.B. Kaner, *Science*, **335**, 1326 (2012); <https://doi.org/10.1126/science.1216744>.
- H. Jeon, J.H. Han, D.M. Yu, J.Y. Lee, T.-H. Kim and Y.T. Hong, *J. Ind. Eng. Chem.*, **45**, 105 (2017); <https://doi.org/10.1016/j.jiec.2016.09.011>.
- Z. Aruna and B.Z. Jang, Process for Producing Nano-Scaled Graphene Platelet Nanocomposite Electrodes for Supercapacitors, U.S. Patent 11/906,786 (2007).
- C. Liu, Z. Yu, D. Neff, A. Zhamu and B.Z. Jang, *Nano Lett.*, **10**, 4863 (2010); <https://doi.org/10.1021/nl102661q>.
- T. Zhai, S. Xie, M. Yu, P. Fang, C. Liang, X. Lu and Y. Tong, *Nano Energy*, **8**, 255 (2014); <https://doi.org/10.1016/j.nanoen.2014.06.013>.
- M. Yu, W. Wang, C. Li, T. Zhai, X. Lu and Y. Tong, *NPG Asia Mater.*, **6**, e129 (2014); <https://doi.org/10.1038/am.2014.78>.
- G. Yu, L. Hu, M. Vosguerichian, H. Wang, X. Xie, J.R. McDonough, X. Cui, Y. Cui and Z. Bao, *Nano Lett.*, **11**, 2905 (2011); <https://doi.org/10.1021/nl2013828>.
- S. Chen, J. Zhu, X. Wu, Q. Han and X. Wang, *ACS Nano*, **4**, 2822 (2010); <https://doi.org/10.1021/nn901311t>.
- L. Khandare and S. Terdale, *Appl. Surf. Sci.*, **418**, 22 (2017); <https://doi.org/10.1016/j.apsusc.2016.12.036>.
- E.R. Ezeigwe, M.T.T. Tan, P.S. Khiew and C.W. Siong, *Ceram. Int.*, **41**, 11418 (2015); <https://doi.org/10.1016/j.ceramint.2015.05.105>.
- D. Hou, H. Tao, X. Zhu and M. Li, *Appl. Surf. Sci.*, **419**, 580 (2017); <https://doi.org/10.1016/j.apsusc.2017.05.080>.
- Z.J. Han, S. Pineda, A.T. Murdock, D.H. Seo, K. Ostrikov and A. Bendavid, *J. Mater. Chem. A Mater. Energy Sustain.*, **5**, 17293 (2017); <https://doi.org/10.1039/C7TA03355A>.
- W. Wang, S. Guo, I. Lee, K. Ahmed, J. Zhong, Z. Favors, F. Zaera, M. Ozkan and C.S. Ozkan, *Sci. Rep.*, **4**, 4452 (2015); <https://doi.org/10.1038/srep04452>.
- V.H. Pham, T.-D. Nguyen-Phan, X. Tong, B. Rajagopalan, J.S. Chung and J.H. Dickerson, *Carbon*, **126**, 135 (2018); <https://doi.org/10.1016/j.carbon.2017.10.026>.
- L. Jiang, Z. Ren, S. Chen, Q. Zhang, X. Lu, H. Zhang and G. Wan, *Sci. Rep.*, **8**, 4412 (2018); <https://doi.org/10.1038/s41598-018-22742-7>.
- X. Zhou, X. Shen, Z. Xia, Z. Zhang, J. Li, Y. Ma and Y. Qu, *ACS Appl. Mater. Interfaces*, **7**, 20322 (2015); <https://doi.org/10.1021/acsami.5b05989>.
- S.A. Pawar, D.S. Patil and J.C. Shin, *J. Ind. Eng. Chem.*, **54**, 162 (2017); <https://doi.org/10.1016/j.jiec.2017.05.030>.
- Y. Zhou, L. Ma, M. Gan, M. Ye, X. Li, Y. Zhai, F. Yan and F. Cao, *Appl. Surf. Sci.*, **444**, 1 (2018); <https://doi.org/10.1016/j.apsusc.2018.03.049>.
- S. Sahoo and J.-J. Shim, *J. Ind. Eng. Chem.*, **54**, 205 (2017); <https://doi.org/10.1016/j.jiec.2017.05.035>.
- B.S. Singu and K.R. Yoon, *J. Ind. Eng. Chem.*, **33**, 374 (2016); <https://doi.org/10.1016/j.jiec.2015.10.036>.
- J.A. Rajesh, J.-H. Park, V.H. Vinh Quy, J.M. Kwon, J. Chae, S.-H. Kang, H. Kim and K.-S. Ahn, *J. Ind. Eng. Chem.*, **63**, 73 (2018); <https://doi.org/10.1016/j.jiec.2018.02.001>.
- B. Zheng, T. Huang, L. Kou, X. Zhao, K. Gopalsamy and C. Gao, *J. Mater. Chem. A Mater. Energy Sustain.*, **2**, 9736 (2014); <https://doi.org/10.1039/C4TA01868K>.
- Q. Chen, Y. Meng, C. Hu, Y. Zhao, H. Shao, N. Chen and L. Qu, *J. Power Sources*, **247**, 32 (2014); <https://doi.org/10.1016/j.jpowsour.2013.08.045>.
- T.M. Higgins, D. McAteer, J.C.M. Coelho, B.M. Sanchez, Z. Gholamvand, G. Moriarty, N. McEvoy, N.C. Berner, G.S. Duesberg, V. Nicolosi and J.N. Coleman, *ACS Nano*, **8**, 9567 (2014); <https://doi.org/10.1021/nn5038543>.
- D.C. Marcano, D.V. Kosynkin, J.M. Berlin, A. Sinitskii, A. Slesarev, Z. Sun, L.B. Alemany, W. Lu and J.M. Tour, *ACS Nano*, **4**, 4806 (2010); <https://doi.org/10.1021/nn1006368>.
- A.M. Shanmugaraj, J.H. Yoon, W.J. Yang and S.H. Ryu, *J. Colloid Interface Sci.*, **401**, 148 (2013); <https://doi.org/10.1016/j.jcis.2013.02.054>.
- S.H. Ryu and A.M. Shanmugaraj, *Chem. Eng. J.*, **244**, 552 (2014); <https://doi.org/10.1016/j.cej.2014.01.101>.
- M.J. Kumar Reddy, S.H. Ryu and A.M. Shanmugaraj, *Nanoscale*, **8**, 471 (2016); <https://doi.org/10.1039/C5NR06680H>.
- T. Szabo, O. Berkesi, P. Forgo, K. Josepovits, Y. Sanakis, D. Petridis and I. Dekany, *Chem. Mater.*, **18**, 2740 (2006); <https://doi.org/10.1021/cm060258+>.
- X. Liu, X. Zhong, Z. Yang, F. Pan, L. Gu and Y. Yu, *Electrochim. Acta*, **152**, 178 (2015); <https://doi.org/10.1016/j.electacta.2014.11.100>.
- C. Xu, J. Sun and L. Gao, *J. Mater. Chem.*, **22**, 975 (2012); <https://doi.org/10.1039/C1JM14099J>.
- Y.G. Li, B. Tan and Y.Y. Wu, *Nano Lett.*, **8**, 265 (2008); <https://doi.org/10.1021/nl0725906>.
- X. Su, L. Yu, G. Cheng, H. Zhang, M. Sun and X. Zhang, *Appl. Energy*, **153**, 94 (2015); <https://doi.org/10.1016/j.apenergy.2014.07.094>.
- M. Toupin, T. Brousse and D. Bélanger, *Chem. Mater.*, **14**, 3946 (2002); <https://doi.org/10.1021/cm020408q>.

54. K. Dai, L. Lu, C. Liang, J. Dai, Q. Liu, Y. Zhang, G. Zhu and Z. Liu, *Electrochim. Acta*, **116**, 111 (2014); <https://doi.org/10.1016/j.electacta.2013.11.036>.
55. X. Su, L. Yu, G. Cheng, H. Zhang, M. Sun, L. Zhang and J. Zhang, *Appl. Energy*, **134**, 439 (2014); <https://doi.org/10.1016/j.apenergy.2014.08.050>.
56. B. Yin, S. Zhang, Y. Jiao, Y. Liu, F. Qu and X. Wu, *CrystEngComm*, **16**, 9999 (2014); <https://doi.org/10.1039/C4CE01302F>.
57. W. Li, X. Cui, R. Zeng, G. Du, Z. Sun, R. Zheng, S.P. Ringer and S.X. Dou, *Sci. Rep.*, **5**, 8987 (2015); <https://doi.org/10.1038/srep08987>.
58. S. Maiti, A. Pramanik and S. Mahanty, *ACS Appl. Mater. Interfaces*, **6**, 10754 (2014); <https://doi.org/10.1021/am502638d>.
59. B.G. Choi, Y.S. Huh, W.H. Hong, H.J. Kim and H.S. Park, *Nanoscale*, **4**, 5394 (2012); <https://doi.org/10.1039/c2nr31215h>.
60. V. Aravindan, W. Chuiling, M.V. Reddy, G.S. Rao, B.V. Chowdari and S. Madhavi, *Phys. Chem. Chem. Phys.*, **14**, 5808 (2012); <https://doi.org/10.1039/c2cp40603a>.
61. B. Anothumakkool, A. Torris A. T, S.N. Bhangé, M.V. Badiger and S. Kurungot, *Nanoscale*, **6**, 5944 (2014); <https://doi.org/10.1039/c4nr00659c>.
62. Z.S. Wu, W. Ren, D.W. Wang, F. Li, B. Liu and H.M. Cheng, *ACS Nano*, **4**, 5835 (2010); <https://doi.org/10.1021/nn101754k>.
63. J. Tao, N. Liu, W. Ma, L. Ding, L. Li, J. Su and Y. Gao, *Sci. Rep.*, **3**, 2286 (2013); <https://doi.org/10.1038/srep02286>.
64. H. Xu, X. Hu, Y. Sun, H. Yang, X. Liu and Y. Huang, *Nano Res.*, **8**, 1148 (2015); <https://doi.org/10.1007/s12274-014-0595-8>.
65. Z. Li, Z. Zhou, G. Yun, K. Shi, X. Lv and B. Yang, *Nanoscale Res. Lett.*, **8**, 473 (2013); <https://doi.org/10.1186/1556-276X-8-473>.
66. H. Chen, S.X. Zhou, M. Chen and L.M. Wu, *J. Mater. Chem.*, **22**, 25207 (2012); <https://doi.org/10.1039/c2jm35054h>.
67. J.T. Zhang, J.W. Jiang and X.S. Zhao, *J. Phys. Chem. C*, **115**, 6448 (2011); <https://doi.org/10.1021/jp200724h>.